

Short note

Volume conservation issues in incompressible smoothed particle hydrodynamics



Prapanch Nair, Gaurav Tomar*

Department of Mechanical Engineering, Indian Institute of Science, Bangalore, India

ARTICLE INFO

Article history:

Received 4 February 2015

Received in revised form 26 May 2015

Accepted 27 May 2015

Available online 3 June 2015

Keywords:

ISPH

Isochoric deformation

Divergence-free velocity

Incompressibility

ABSTRACT

A divergence-free velocity field is usually sought in numerical simulations of incompressible fluids. We show that the particle methods that compute a divergence-free velocity field to achieve incompressibility suffer from a volume conservation issue when a finite time-step position update scheme is used. Further, we propose a deformation gradient based approach to arrive at a velocity field that reduces the volume conservation issues in free surface flows and maintains density uniformity in internal flows while retaining the simplicity of first order time updates.

© 2015 Elsevier Inc. All rights reserved.

1. Introduction

Particle methods are becoming increasingly popular in simulating incompressible fluid flows with complex geometries and interfaces. To achieve incompressibility, particle methods either use weak compressibility models [1,2] or solve a linear system for a pressure field [3,4]. In the latter class of methods, the source term for the pressure equation is either a function of density variation (or number density) [5,6] or a function of the divergence of velocity [7,3] or a mixed formulation [8,9]. A divergence-free condition on velocity for incompressibility, following Eulerian simulation methods, is known to produce smoother pressure fields as compared to methods employing density based source terms. However, recent studies have addressed the density errors [10–12] observed when a divergence free velocity condition is used, and attributed the cause of these errors to particle configurations [8] and the accuracy of the Laplacian operator [12].

In the present study, we show that the choice of temporal update scheme also plays a crucial role in ensuring volume conservation and thereby ensuring incompressibility. We demonstrate accumulation of severe volume conservation errors when a divergence free velocity field is set as a constraint for incompressibility in first order time update schemes which are popularly used in Smoothed Particle Hydrodynamics (SPH) among other particle based methods.

The computations of acceleration of particles involve several particle–particle interactions and are therefore computationally expensive. Hence, first order Eulerian update and the second order Predictor–Corrector approach introduced by Cummins and Rudman [3] are widely used to solve problems of practical size using SPH. We derive a new pressure equation based on isochoricity condition on a fluid element (particle). The method is based on computation of deformation gradient field of the particle configuration ensuring that the Jacobian of the deformation remains unity which is essentially the condition for isochoricity.

* Corresponding author.

E-mail address: gtom@mecheng.iisc.ernet.in (G. Tomar).

2. Incompressible SPH formulation

The momentum and mass conservation equations, in the Lagrangian frame of reference, describing isothermal fluid flows are

$$\frac{d\mathbf{u}}{dt} = \frac{1}{\rho} \left(-\nabla p + \nabla \cdot (2\mu\mathbf{D}) + \mathbf{f}^B \right), \text{ and} \quad (1)$$

$$\frac{1}{\rho} \frac{d\rho}{dt} = -\nabla \cdot \mathbf{u} \quad (2)$$

respectively. Here \mathbf{u} , p , ρ , and μ are the velocity, pressure, density and coefficient of dynamic viscosity, respectively. Also, $\mathbf{D} = (\nabla\mathbf{u} + \nabla\mathbf{u}^T)/2$ is the deformation rate tensor, \mathbf{f}^B is the body force on the fluid element. The operator d/dt denotes the material derivative. For incompressible fluids, the material derivative of density is zero and therefore, condition for incompressibility is given by $\nabla \cdot \mathbf{u} = 0$. Mesh based algorithms (for e.g. projection methods) seek a pressure field (p) at each time step that renders a solenoidal velocity field.

Following this idea, mesh-free particle methods such as Incompressible Smoothed Particle Hydrodynamics (ISPH) [3,4,13], some versions of Moving Particle Semi-implicit (MPS) [7] employ computation of a divergence free velocity field to achieve incompressibility. In ISPH, an intermediate velocity field (\mathbf{u}^*) is first computed based on viscous and body forces. The pressure Poisson equation, given by

$$\nabla \cdot \left(\frac{\nabla p}{\rho} \right) = \frac{\nabla \cdot \mathbf{u}^*}{\Delta t}, \quad (3)$$

is then solved with the divergence of the intermediate velocity field acting as the source term. Here Δt is the time step used for temporal updates, and is chosen based on the Courant–Friedrich–Lewy (CFL) condition for stability. The pressure gradient is then obtained from the solution to this linear system. This procedure is akin to projection method based algorithms on Eulerian grids. Different time integration schemes can be employed to solve Eqs. (1) and (3) such as first order Euler time update (see [4]) and predictor corrector (see [3]). In what follows, we discuss the volume conservation issues due to the finite time stepping used in these methods.

3. Volume loss

A divergence-free velocity field *does not* truly represent incompressibility in the Lagrangian context when finite time-steps are used. To demonstrate this, we consider a given divergence-free velocity field, \mathbf{u}_{DF} , to advect particles that represent a fluid domain and check its volume conservation. Consider the first-order Euler update scheme from time step n to $n+1$. The position vector is updated as,

$$\mathbf{r}^{n+1} = \mathbf{r} + \Delta t \mathbf{u}_{DF}. \quad (4)$$

The corresponding gradient of this deformation can be written as,

$$\mathbf{F}^{n+1} = \mathbf{I} + \Delta t \nabla \mathbf{u}_{DF}. \quad (5)$$

For a strictly incompressible flow evolution, this deformation remains isochoric and hence the determinant of the deformation gradient tensor \mathbf{F} is unity [14]. Therefore,

$$\det(\mathbf{I} + \Delta t \nabla \mathbf{u}_{DF}) = 1 \quad (6)$$

For a 3-dimensional flow, Eq. (6) can be expanded (using Cayley–Hamilton theorem) to,

$$\Delta t I_1 + \Delta t^2 I_2 + \Delta t^3 I_3 = 0, \quad (7)$$

where I_1 , I_2 and I_3 are the first, second and third invariants (I_3 being the determinant) of the tensor $\nabla \mathbf{u}_{DF}$. Similarly, for 2-dimensional flows we have,

$$\Delta t I_1 + \Delta t^2 I_2 = 0. \quad (8)$$

Here,

$$I_1 = \text{tr} \nabla \mathbf{u}_{DF} = \nabla \cdot \mathbf{u}_{DF} = 0,$$

and the remaining terms of Eq. (7) would vanish only for a vanishing Δt . Hence, for finite time-steps, the terms corresponding to the second and third invariants of the displacement gradient tensor, $\nabla \mathbf{u}_{DF}$, constitute errors in volume conservation. For finite Δt , in two-dimensional flows, the area ratio between two successive time steps is given by,

$$A^{n+1}/A^n = \det \mathbf{F}^{n+1} \quad (9)$$

$$= 1 + \underbrace{\Delta t I_1 + \Delta t^2 I_2}_0 \quad (10)$$

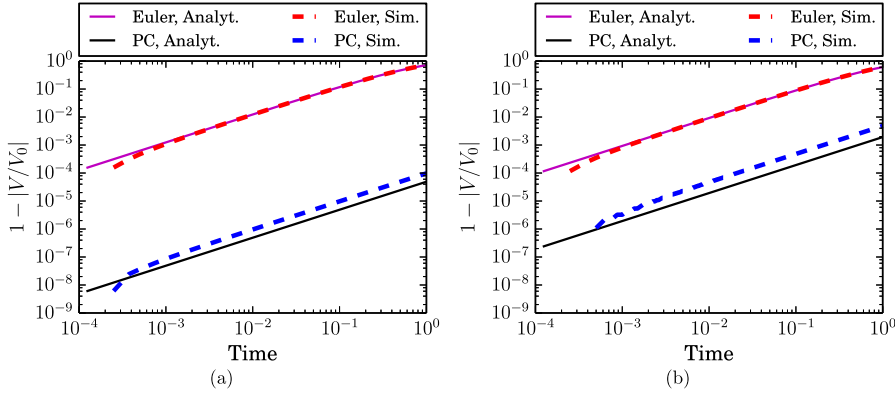


Fig. 1. Change in volume of (a) a 2D elliptical droplet and (b) 3D ellipsoidal droplet with time using the first order Euler update and the predictor–corrector (PC) update.

At time $t = m\Delta t$, the area ratio with respect to the initial area, $A(0)$, is

$$A(t)/A(0) = \left(1 + \Delta t^2 I_2\right)^m, \quad (11)$$

which indicates a logarithmic reduction in volume/area.

A similar analysis can be performed for the predictor–corrector time update given by Ref. [3] (see Appendix A). For a spacially linear, steady velocity field, the deformation gradient can be written as,

$$\mathbf{F}^{n+1} = \mathbf{I} + \Delta t \nabla \mathbf{u}_{DF}^n + \Delta t^2 (\nabla \mathbf{u}_{DF}^n)^2 / 2 + O(\Delta t^3). \quad (12)$$

For predictor–corrector position updates, the ratio of area at time t to the initial area (note that for three dimensions we would be computing the volume), is given by,

$$A(t)/A(0) = \left(1 + \Delta t G_1 + \Delta t^2 G_2\right)^m, \quad (13)$$

where G_1 and G_2 are the first and second invariants of the tensor $\nabla \mathbf{u}_{DF}^n + \Delta t (\nabla \mathbf{u}_{DF}^n)^2 / 2$.

To illustrate the above, we choose a divergence-free velocity field given by,

$$\mathbf{u} = -100x\hat{\mathbf{i}} + 100y\hat{\mathbf{j}}. \quad (14)$$

For an initial particle spacing of $\Delta x = 0.05$ and a time step $\Delta t = 1.25 \times 10^{-4}$ (which is within the CFL limits at the initial stage), the theoretical value of the slope of area reduction (in log–log scale), given by Eq. (12), is -1.25 . Similarly, the slope of the area change for predictor–corrector algorithm (Eq. (13)) amounts to 4.88×10^{-5} . The above theoretical slopes can be compared with the measured change in area/volume from the simulation of the elliptic drop deforming under the given divergence-free velocity field. The analytical predictions and the simulated volume drop agree well as shown in Fig. 1(a).

To perform a validation in three dimensions, we consider volume change during the simulation of an ellipsoid drop with a divergence free velocity field

$$\mathbf{u} = 100x\hat{\mathbf{i}} - 50y\hat{\mathbf{j}} - 50z\hat{\mathbf{k}}, \quad (15)$$

where $\hat{\mathbf{i}}, \hat{\mathbf{j}}, \hat{\mathbf{k}}$ are the unit vectors along $\mathbf{x}, \mathbf{y}, \mathbf{z}$ respectively. The slope of the volume change for Eulerian updates amounts to -0.93 .

The slope for predictor–corrector in two-dimensions is quite low $\sim 10^{-5}$, however for position updates in three-dimensions, the error increases by two orders to 1.92×10^{-3} (see Fig. 1(b)). Fig. 1 clearly demonstrates the loss of volume incurred during position updates, even while using a divergence-free velocity field, with finite time-step based algorithms prevalent in the literature.

In what follows, we present a different definition of volume conservation for particle methods and based on it we derive a new pressure equation.

4. Deformation gradient based pressure equation

Error in volume conservation discussed in the previous section may lead to pressure fluctuations leading to instabilities in the simulation in addition to other numerical inaccuracies due to truncation errors, kernel approximations and particle configurations. The issue of volume conservation has also been discussed in the literature but always in the context of density errors [12,11,10]. We argue that instead of the traditional divergence free condition on the velocity to satisfy incompressibility, the particle configuration can be constrained to evolve *isochorically*.

In order to enforce isochoricity at each time step, we begin with a condition for isochoric deformation based on the deformation gradient of the fluid. Essentially, we seek an isochoric particle configuration \mathbf{r}^{n+1} from the configuration \mathbf{r}^n . Assuming Δt is the time step that satisfies the CFL criterion ($\Delta t < \alpha \Delta x / U_{\max}$; where α is the CFL number), we may perform a first order Euler time integration to get the particle configuration at $n + 1$:

$$\mathbf{r}^{n+1} = \mathbf{r}^n + \Delta t \mathbf{u}^{n+1}. \quad (16)$$

The velocity vector, \mathbf{u}^* , (obtained by an explicit update of the momentum equations) can be split into two components using Helmholtz decomposition as $\mathbf{u}^{n+1} = \tilde{\mathbf{u}} + \mathbf{u}^{n+1}$. Here \mathbf{u}^{n+1} is divergence free and $\tilde{\mathbf{u}}$ is irrotational and therefore, can be written as a gradient of a scalar $\tilde{\mathbf{u}} = \nabla \phi$. Thus, writing the correction to \mathbf{u}^* to obtain \mathbf{u}^{n+1} as $\tilde{\mathbf{u}}$, the above update rule can be written as,

$$\mathbf{r}^{n+1} = \mathbf{r}^n + \Delta t (\mathbf{u}^* + \tilde{\mathbf{u}}). \quad (17)$$

For a particle configuration representing incompressible flow with constant density particles we require this deformation (change in the particle configuration) to occur isochorically. Assuming \mathbf{r}^n to be the initial configuration and taking gradient on both sides of Eq. (17), the condition for isochoricity is given by Eq. (7) for 3D (and Eq. (8) for 2D). For a vanishing $\Delta t \rightarrow 0$, the condition in Eq. (7) reduces to $I_1 = 0$, that is,

$$\text{tr} \nabla \mathbf{u}^* + \text{tr} \nabla \tilde{\mathbf{u}} = 0, \quad (18)$$

$$\implies \nabla \cdot \mathbf{u}^* = -\nabla \cdot \tilde{\mathbf{u}} \quad (19)$$

The above relation yields the pressure Poisson equation (Eq. (3)) used in earlier ISPH schemes.

Equations (7) and (8) are the conditions for true isochoric motion in particle based methods that use a finite time-step for updating particle positions. Clearly, using Eq. (19) leads to particle configurations which do not strictly conserve volume.

Writing $\tilde{\mathbf{u}} = \Delta t \nabla p / \rho$, an equation for pressure field, using the condition $\det(\mathbf{I} + \Delta t \nabla \mathbf{u}) = 1$, can be obtained as,

$$1 = \det((\mathbf{I} + \Delta t \nabla \mathbf{u}^*) + \Delta t \nabla \tilde{\mathbf{u}}) \quad (20)$$

$$= \det\left(\mathbf{A} + \frac{\Delta t^2}{\rho} \nabla(\nabla p)\right) \quad (21)$$

$$= \det \mathbf{A} + \text{cof}(\mathbf{A}) : \frac{\Delta t^2}{\rho} \nabla(\nabla p) + \mathcal{O}(\Delta t^4) \quad (22)$$

where, $\mathbf{A} = \mathbf{I} + \Delta t \nabla \mathbf{u}^*$, with elements a_{ij} and $\text{cof}(\mathbf{A})$ denotes the cofactor tensor of \mathbf{A} . The higher order term in the above equation is

$$\mathcal{O}(\Delta t^4) \equiv \frac{\Delta t^4}{\rho^2} \det \nabla(\nabla p)$$

for two dimensions, and

$$\mathcal{O}(\Delta t^4) \equiv \frac{\Delta t^4}{\rho^2} \mathbf{A} : \text{cof}(\nabla(\nabla p)) + \frac{\Delta t^6}{\rho^3} \det(\nabla(\nabla p))$$

for three dimensions. For a 2D domain, simplifying the above equation and neglecting the higher order terms, we get

$$1 - \det \mathbf{A} = \frac{\Delta t^2}{\rho} \left(a_{22} \frac{\partial^2 p}{\partial x^2} + a_{11} \frac{\partial^2 p}{\partial y^2} - (a_{12} + a_{21}) \frac{\partial^2 p}{\partial x \partial y} \right). \quad (23)$$

For 2D flows, $(1 - \det \mathbf{A}) \sim \mathcal{O}(\Delta t^2)$ and therefore the above equation is essentially second order accurate. For 3D, a similar derivation results in the following second-order differential equation for pressure:

$$\begin{aligned} 1 - \det \mathbf{A} = \frac{\Delta t^2}{\rho} & \left((a_{22}a_{33} - a_{23}a_{32}) \frac{\partial^2 p}{\partial x^2} + (a_{11}a_{33} - a_{31}a_{13}) \frac{\partial^2 p}{\partial y^2} + (a_{11}a_{22} - a_{21}a_{12}) \frac{\partial^2 p}{\partial z^2} \right. \\ & - (a_{12}a_{33} + a_{21}a_{33} - a_{13}a_{32} - a_{23}a_{31}) \frac{\partial^2 p}{\partial x \partial y} + (a_{12}a_{23} + a_{21}a_{32} - a_{22}a_{31} - a_{13}a_{22}) \frac{\partial^2 p}{\partial x \partial z} \\ & \left. - (a_{11}a_{23} + a_{11}a_{32} - a_{21}a_{13} - a_{12}a_{31}) \frac{\partial^2 p}{\partial y \partial z} \right) \end{aligned} \quad (24)$$

Note that Eqs. (23) and (24) have mixed derivatives with small coefficients in comparison to the coefficients of “unmixed” second order derivatives and therefore the above equations remain elliptic. Using the previous time-step configuration as the reference configuration to obtain the deformation gradient \mathbf{F} (Eq. (12)), the new formulation is given by Algorithm 1 for Incompressible Smoothed Particle Hydrodynamics (ISPH).

Data: Particle positions \mathbf{r}^n , velocities \mathbf{u}^n at time-step n

Result: Updated \mathbf{r}^{n+1} , \mathbf{u}^{n+1}

while $t < \text{end time}$ **do**

$\mathbf{u}^* \leftarrow \mathbf{u}^n + \Delta t (\nabla \cdot (\nu \nabla \mathbf{u}^n) + \mathbf{f}^b)$

$\Delta \mathbf{r}^* \leftarrow \Delta t \mathbf{u}^*$

$\mathbf{A} \leftarrow \mathbf{I} + \nabla(\Delta \mathbf{r}^*)$

$p \leftarrow$ solution of Eq. (23) in 2D and Eq. (24) in 3D

$\mathbf{u}^{n+1} \leftarrow \mathbf{u}^* - \Delta t (\nabla p / \rho)$

$\mathbf{r}^{n+1} \leftarrow \mathbf{r}^n + \Delta t \mathbf{u}^{n+1}$

$t \leftarrow t + \Delta t$

$n \leftarrow n + 1$

end

Algorithm 1: Deformation gradient based ISPH (DG-SPH) algorithm.

The second order derivatives of pressure are approximated in SPH [15] as:

$$\left. \frac{\partial^2 p}{\partial x^i \partial x^j} \right|_a = \sum_b \frac{m_b}{\rho_b} \left(4 \frac{\Delta x^i \Delta x^j}{\Delta r^2} - \delta^{ij} \right) (p_a - p_b) F_{ab}, \quad (25)$$

and the deformation gradient tensor can be obtained as:

$$\mathbf{F}_a^{ij} = \delta_{ij} + \sum_b \left(\mathbf{r}_b^j - \mathbf{r}_a^j \right) \nabla W_{ab}^i \frac{m_b}{\rho_b}, \quad (26)$$

where b represents the particles in the neighborhood of the particle a , $W_{ab} = W(\mathbf{r}_a - \mathbf{r}_b, h)$, $F_{ab} = \mathbf{r}_{ab} \cdot \nabla W_{ab} / (|\mathbf{r}_{ab}|^2 + (0.01h)^2)$ and the indices i and j are the coordinate indices. Here, δ_{ij} is the identity tensor and the second term on the right represents the *displacement gradient* tensor.

In order to illustrate the volume conservation issues in particle methods for free surface and internal flows that exemplify scenarios encountered in common applications, we use the above discussed DG-SPH method and compare with the 1st order Euler and also second order Predictor–Corrector schemes for the standard ISPH. We note here that the mixed derivatives in the pressure equation in DG-SPH result in a slight increase in the computational cost ($\sim 5\%$). The volume loss/gain manifests as change in volume along with a density change in free-surface flows, whereas in internal flows although the volume remains conserved the density varies across the domain (see Ref. [10]).

In what follows, we show ISPH results for a deforming ellipsoid to show volume conservation issue in free surface flow simulations and later we also discuss density errors observed for an internal flow problem, namely the lid driven cavity.

5. Free surface flows: deforming ellipsoid

First, we point at the deficiency of the first order Euler update as derived in Section 1. As opposed to Section 1 where a given divergence free velocity field was used, we solve for the velocity field in this section. The following kernel is used for simulations in the present section:

$$W(q) = \frac{\alpha_d}{h^d} \begin{cases} (3-q)^5 - 6(2-q)^5 + 15(1-q)^5 & 0 \leq q < 1 \\ (3-q)^5 - 6(2-q)^5 & 1 \leq q < 2 \\ (3-q)^5 & 2 \leq q < 3 \end{cases}. \quad (27)$$

Here $q = r/h$, where r is the distance between particles, d is the number of spatial dimensions and h is the smoothing distance and is taken as 1.3 times the initial particle spacing. The renormalization coefficient α_d takes the values $7/(478\pi)$ and $3/(359\pi)$, as outlined in Ref. [16], for 2D and 3D cases, respectively. The details of the implementation of the ISPH algorithm used here are present in Ref. [17]. Later, we would also employ, to demonstrate the sensitivity of predictor–corrector update with different kernels, the Wendland kernel given by:

$$W(q) = \frac{\alpha_d}{h^d} \left(1 - \frac{q}{2} \right)^4 (2q + 1) \quad 0 \leq q < 2 \quad (28)$$

Here α is given as $7/(4\pi)$ and $21/(16\pi)$ for 2D and 3D simulations respectively as in [18].

For the test case presented in this section, a prolate ellipsoid (and an ellipse in 2D) deforming into an oblate ellipsoid inertially due to a divergence free initial velocity field is simulated. For the ellipse, the geometry given by

$$x^2 + y^2/0.7^2 = 1 \quad (29)$$

is chosen, and an initial velocity field of $\mathbf{u} = -100x\hat{\mathbf{i}} + 100y\hat{\mathbf{j}}$ is used. The volume of the geometry is measured as the drop deforms until the extent of the drop along the minor axis becomes equivalent to the initial major axis. A rectangular array of particles with initial spacing of 0.025 with a smoothing length 1.3 times this spacing and the quintic spline kernel given by Eq. (27) is used in this simulation. Simulation is performed with a time step of 0.0002 for a duration of 0.003 time units.

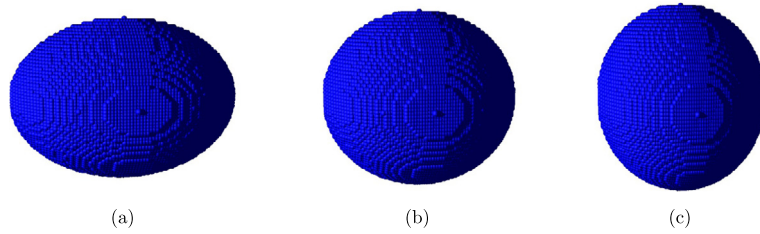


Fig. 2. 3D prolate ellipsoid deforming to oblate under an initial divergence free velocity field: (a) $t = 0$, (b) $t = 0.0016$ and (c) $t = 0.003$.

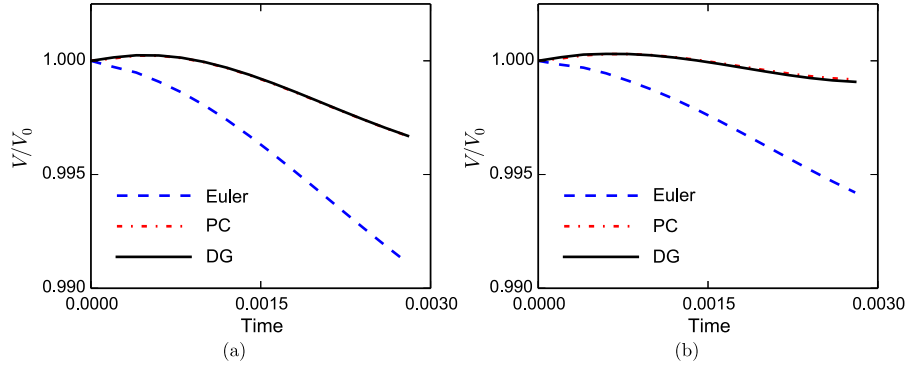


Fig. 3. Change in volume of (a) a 2D elliptical droplet, (b) 3D prolate ellipsoidal droplet with time using the first order Euler update, the predictor–corrector (PC) update and using the introduced Deformation Gradient (DG) based update.

To study volume loss in three dimensional problems, we simulate a three dimensional prolate spheroid given by

$$x^2 + y^2/0.7^2 + z^2/0.7^2 = 1 \quad (30)$$

with an initial velocity field of $\mathbf{u} = -100x\hat{\mathbf{i}} + 50y\hat{\mathbf{j}} + 50z\hat{\mathbf{k}}$. This initial velocity field deforms the initial prolate spheroid (aligned along the horizontal axis as shown in Fig. 2(a)) into an oblate spheroid as shown in Fig. 2(c). The time step size, time duration, particle spacing and kernel choices are all chosen to be similar to those in the 2D ellipse geometry. Since the simulations involve solving for pressure with a free surface, Dirichlet boundary conditions have to be imposed at the free surface. We choose the recently proposed model in Ref. [17] for simulating the free surface. The change in volume with time is shown in Fig. 3 and the corresponding shape of the deforming ellipsoid in 3D at three different times is shown in Fig. 2. Simulation with the Euler update scheme shows appreciable volume loss in both 2D and 3D cases. Both DG-SPH and Predictor–Corrector schemes being 2nd order accurate show better volume conservation.

6. Internal flows: lid driven cavity

Volume conservation errors aggravate density fluctuations in internal flow problems in particle methods. To demonstrate this, we simulate the Lid Driven Cavity (LDC) flow with Reynolds numbers 400 and 1000. First, we show that the simulation results of lid-driven cavity flow using the proposed DG-SPH are in good agreement with Ghia et al. [19]. Fig. 4(a) shows that grid (number of particles) convergence is achieved for a modest resolution of 100×100 particles for $Re = 400$. Fig. 4(b) shows that, for $Re = 1000$ good agreement with Ghia et al. is achieved with a particle resolution of 200×200 . The present results are also in agreement with the state of the art in SPH literature (see [10] and [20]).

To highlight the volume conservation/density uniformity issue in the different schemes discussed in this study, we perform simulations in a square cavity of unit size with an initial particle spacing of $\Delta x = 0.02$. Since the choice of kernel plays a major role in accuracy of derivatives in SPH, we have chosen two kernel functions, the quintic spline function [16] and the Wendland [18] kernels discussed in Section 5. The ghost particle boundary conditions described by Scewz et al. [10] are used for walls and corners in these simulations. Figs. 5 and 6 compare the different algorithms and kernel functions against the results by Ghia et al. [19]. The wall bounded nature of this test case prevents the volume conservation errors from escalating like in the case of free surface flows. However, such errors manifest as errors in the density. The density errors accumulate and cause instabilities and may affect the flow field severely. The root mean square of the relative errors in density are computed by

$$\hat{\rho}_a = \sum_b m_b W(|\mathbf{r}_a - \mathbf{r}_b|, h) \quad (31)$$

on a uniform array of points (subscript a represents points on the array and b represents the actual SPH particles). The RMS of the relative density errors are plotted against time in Figs. 7 and 9.

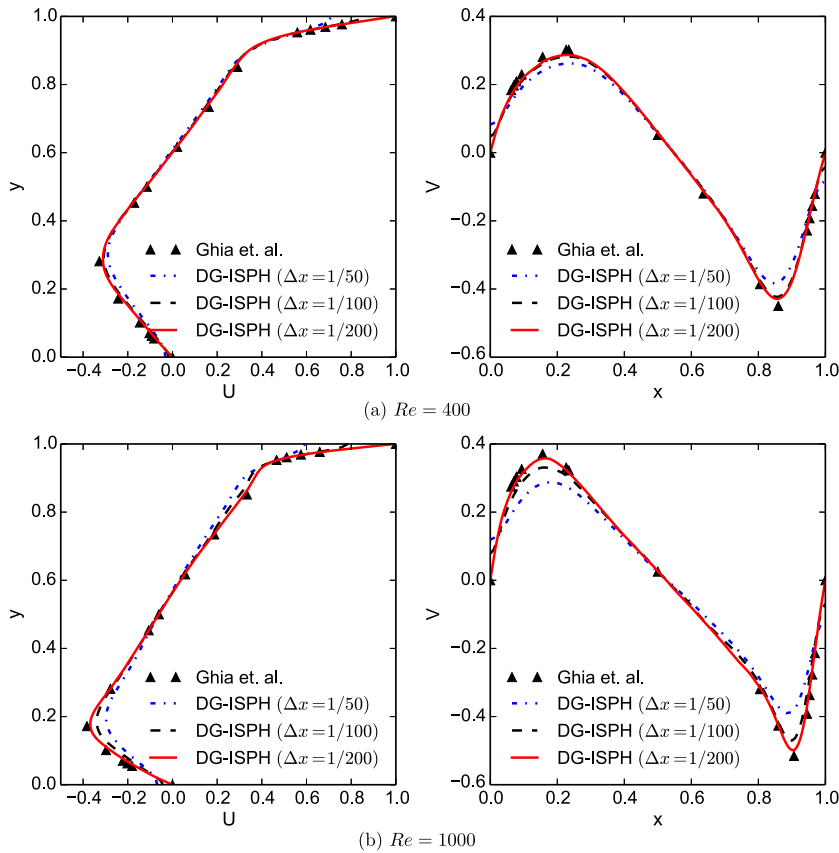


Fig. 4. Velocity profiles of lid driven cavity flow using the proposed DG-ISPH with three different initial particle spacings, compared with Finite Volume results of Ghia et al. [19], for Reynolds numbers 400 and 1000.

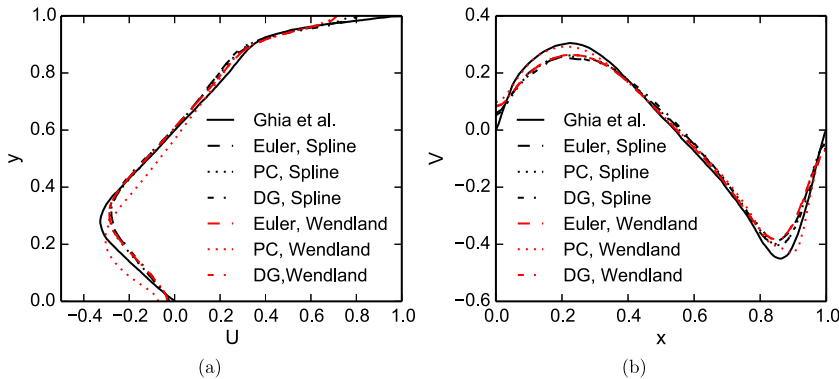


Fig. 5. Comparison of simulations of lid driven cavity flow, with those of Ghia et al. [19], for Reynolds number 400. Red colored lines indicate simulations with the Wendland kernel. (Note that the simulation is performed with 2500 particles.) (For interpretation of the references to color in this figure legend, the reader is referred to the web version of this article.)

Note that the RMS error over the whole domain reflects only on the average density error in the domain. As the lid starts driving the flow, due to viscous forces, the particles have a tendency to ‘crowd’ towards the downstream corner and increase the apparent density. Fig. 8 shows the distribution of the error in density in the cavity. Clearly, simulations performed with isochoricity conditions, that is with the proposed DG-ISPH, have minimum variation in the density. Surprisingly, the performance of the second order PC scheme is even worse than the first Euler method, with reference to errors in density. This reflects on the accuracy of the simulation (note the plots in Figs. 5 and 6, where the PC scheme behaves differently) as well. The errors become even more severe with increase in the Reynolds number. In comparison, the proposed DG-ISPH schemes shows a slight increase only in the downstream corner of the cavity which could be a result of the imposition of the boundary conditions at the walls, especially in the corners, and deserves separate attention.

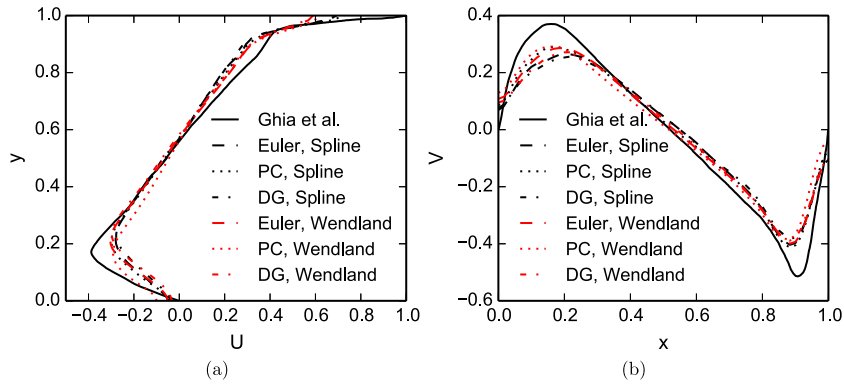


Fig. 6. Comparison of simulations of lid driven cavity flow, with those of Ghia et al. [19], for Reynolds number 1000. Red colored lines indicate simulations with the Wendland kernel. (Note that the simulation is performed with 2500 particles.) (For interpretation of the references to color in this figure legend, the reader is referred to the web version of this article.)

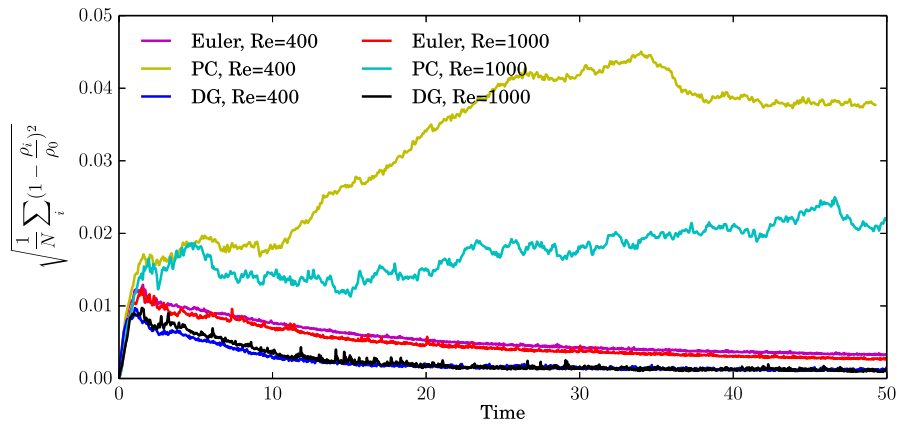


Fig. 7. RMS of relative density errors in Lid Driven Cavity simulations using the Wendland kernel.

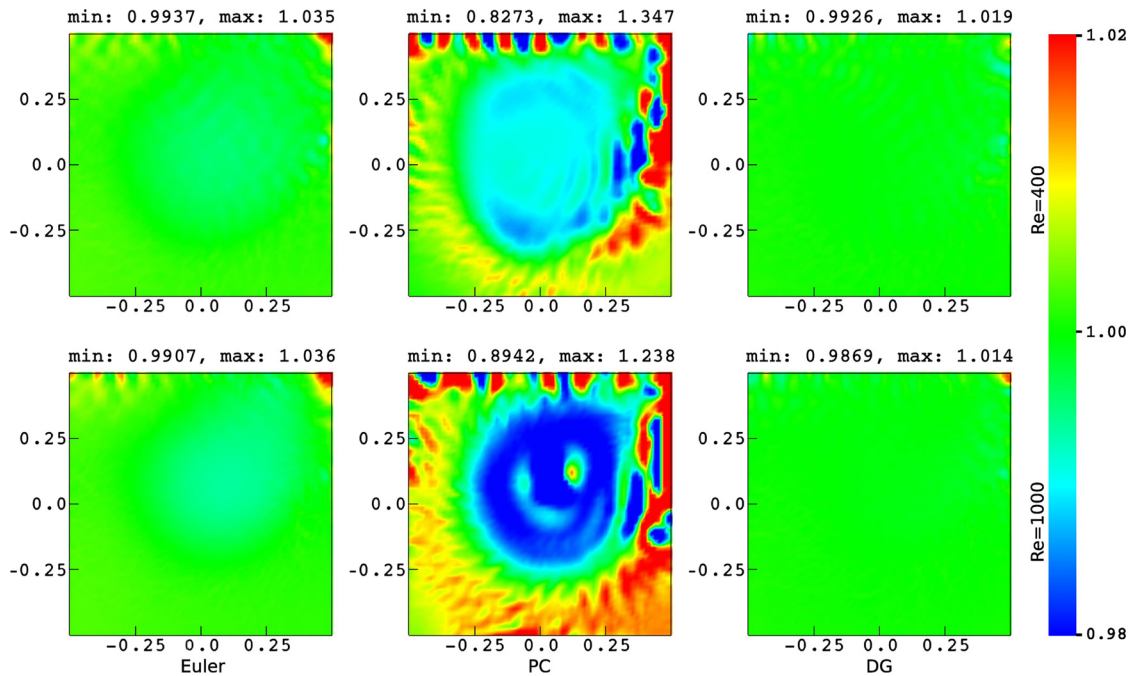


Fig. 8. Computed density contours at $t = 45$. Kernel used is 5th order Wendland kernel.

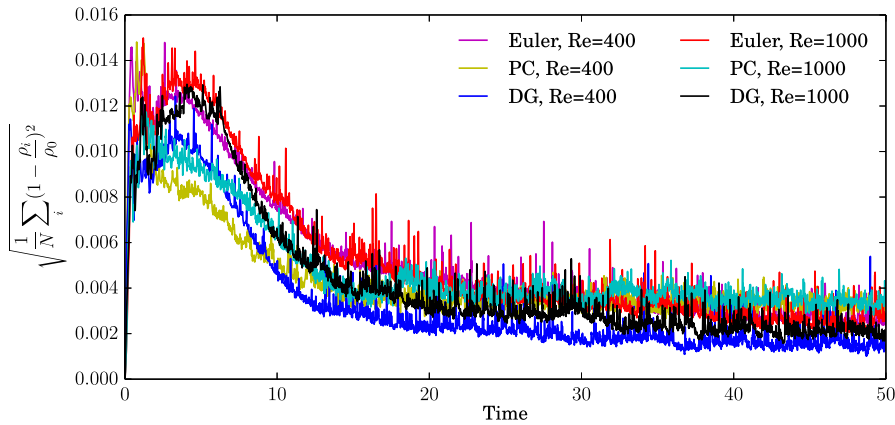


Fig. 9. RMS of relative density errors in Lid Driven Cavity simulations using the Quintic Spline kernel.

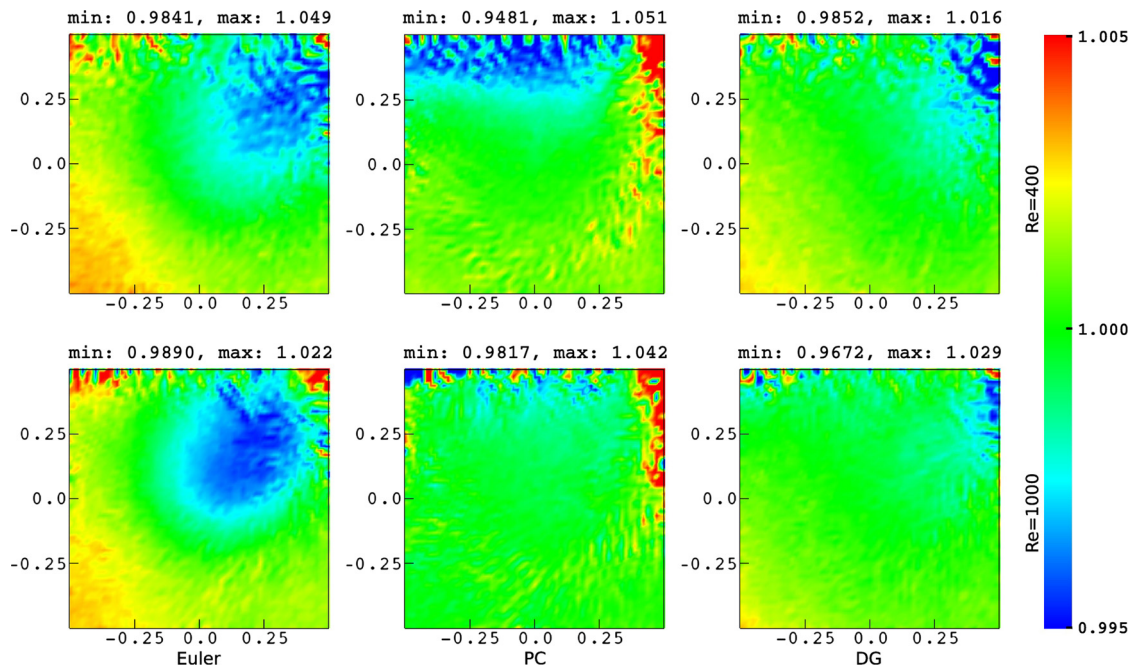


Fig. 10. Computed density contours at $t = 45$. Kernel used is the Quintic Spline kernel.

Interestingly, when we use a quintic spline kernel (Eq. (27)) we observe (see Figs. 9 and 10) that the first-order Euler and the DG schemes show an increase in the density errors whereas the predictor–corrector scheme shows a decrease in the error when compared to the results with Wendland kernel (see Fig. 8). However, the error for DG-ISPH is still smaller compared to the ISPH scheme with both first-order Euler and predictor–corrector scheme. The dependence of accuracy of different update schemes on the kernel functions is an unexplored area and we plan to address it in our future work.

7. Conclusion

First-order Euler and predictor–corrector time update schemes are widely used in particle methods simulating incompressible fluid flows. We have illustrated that a divergence free velocity as a condition for incompressibility results in volume conservation errors when finite time-steps for particle position updates are used. We argue that special attention is required while employing particle methods for simulating incompressible flows. Based on these observations, we suggest that the deformation of the particle configurations during flow evolution must evolve isochorically, a requirement similar to the satisfaction of discretized incompressibility condition on Eulerian grids. Employing a deformation gradient tensor of the particle configuration, we derive a pressure equation that satisfies isochoricity of the particle distribution.

We validate the proposed scheme using the free surface case of a deforming ellipsoid (and ellipse in 2D) and using the Lid Driven Cavity flow. The new algorithm is shown to outperform methods using PPE with Eulerian time updates in all

the cases considered in this study. The algorithm is also compared with the Predictor–Corrector algorithm of Cummins [3] widely used in ISPH literature, and is shown to be consistent in its ability to reduce volume conservation errors. Where the density errors are distributed in the entire domain for the first order Euler and predictor–corrector schemes, DG-ISPH shows errors only near the walls, in particular close to the downstream corner. This could be due to boundary condition model used at the walls and deserves special attention. Nevertheless, the RMS error clearly shows that the overall error in density is significantly reduced (see Figs. 7 and 9).

Appendix A

The Predictor–Corrector algorithm given by Cummins and Rudman [3] is describe in Algorithm 2.

Data: Particle positions \mathbf{r}^n , velocities \mathbf{u}^n at time-step n

Result: Updated \mathbf{r}^{n+1} , \mathbf{u}^{n+1}

while $t < \text{end time}$ **do**

```

     $\mathbf{r}' = \mathbf{r}^n + \Delta t \mathbf{u}^n$ 
     $\mathbf{u}^* \leftarrow \mathbf{u}^n + \Delta t (\nabla \cdot (\nu \nabla \mathbf{u}^n) + \mathbf{f}^B)$ 
     $p \leftarrow \text{solution of SPH approximation to Eq. (3)}$ 
     $\mathbf{u}^{n+1} \leftarrow \mathbf{u}^* - \Delta t (\nabla p / \rho)$ 
     $\mathbf{r}^{n+1} \leftarrow \mathbf{r}^n + \Delta t (\mathbf{u}^n + \mathbf{u}^{n+1}) / 2$ 
     $t \leftarrow t + \Delta t$ 
     $n \leftarrow n + 1$ 

```

end

Algorithm 2: Predictor–Corrector ISPH algorithm [3].

Based on the above algorithm, we have

$$\begin{aligned} \mathbf{r}' &= \mathbf{r}^n + \Delta t \mathbf{u}^n \\ \mathbf{r}^{n+1} &= \mathbf{r}^n + \frac{\Delta t}{2} (\mathbf{u}^n + \mathbf{u}^{n+1}|_{\mathbf{r}'}) \end{aligned}$$

The velocity $\mathbf{u}^{n+1}|_{\mathbf{r}'}$ can be written as:

$$\begin{aligned} \mathbf{u}^{n+1}|_{\mathbf{r}'} &= \mathbf{u}^{n+1}|_{\mathbf{r}^n} + \nabla \mathbf{u}^{n+1}|_{\mathbf{r}^n} \cdot (\mathbf{r}' - \mathbf{r}^n) + O((\mathbf{r}' - \mathbf{r}^n)^2) \\ &= \mathbf{u}^{n+1}|_{\mathbf{r}^n} + \nabla \mathbf{u}^{n+1}|_{\mathbf{r}^n} \cdot (\Delta t \mathbf{u}^n) + O(\Delta t^2) \end{aligned}$$

Taking gradient $\nabla_{\mathbf{r}^n} \mathbf{r}^{n+1}$ with respect to the particle configuration \mathbf{r}^n ,

$$\begin{aligned} \mathbf{F} &= \mathbf{I} + \frac{\Delta t}{2} (\nabla_{\mathbf{r}^n} \mathbf{u}^n + \nabla_{\mathbf{r}^n} \mathbf{u}^{n+1}|_{\mathbf{r}'}) \\ &= \mathbf{I} + \frac{\Delta t}{2} (\nabla_{\mathbf{r}^n} \mathbf{u}^n + \nabla_{\mathbf{r}^n} \mathbf{u}^{n+1}|_{\mathbf{r}^n} + \Delta t \nabla (\nabla \mathbf{u}^{n+1} \cdot \mathbf{u}^n) + O(\Delta t^2)) \\ &= \mathbf{I} + \frac{\Delta t}{2} \nabla (\mathbf{u}^n + \mathbf{u}^{n+1}) + \frac{\Delta t^2}{2} (\nabla \nabla \mathbf{u}^{n+1} \cdot \mathbf{u}^n + \nabla \mathbf{u}^{n+1} \cdot \nabla \mathbf{u}^n) + O(\Delta t^3) \\ &= \mathbf{I} + \Delta t \nabla \mathbf{u}^n + \frac{\Delta t^2}{2} \nabla \mathbf{u}^{n+1} \cdot \nabla \mathbf{u}^n + \frac{\Delta t^2}{2} (\nabla \nabla \mathbf{u}^n) \cdot \mathbf{u}^n + O(\Delta t^3) \end{aligned}$$

For a spacially linear, steady velocity field,

$$\mathbf{F} = \mathbf{I} + \Delta t \nabla \mathbf{u}^n + \frac{\Delta t^2}{2} (\nabla \mathbf{u}^n)^2 + O(\Delta t^3)$$

References

- [1] J.J. Monaghan, Smoothed particle hydrodynamics, *Annu. Rev. Astron. Astrophys.* 30 (1992) 543–574.
- [2] A. Das, P. Das, Bubble evolution through submerged orifice using smoothed particle hydrodynamics: basic formulation and model validation, *Chem. Eng. Sci.* 64 (10) (2009) 2281–2290.
- [3] S.J. Cummins, M. Rudman, An SPH projection method, *J. Comput. Phys.* 152 (2) (1999) 584–607.
- [4] E.-S. Lee, C. Moulinec, R. Xu, D. Violeau, P. Stansby, Comparisons of weakly compressible and truly incompressible algorithms for the SPH mesh free particle method, *J. Comput. Phys.* 227 (18) (2008) 8417–8436.
- [5] S. Shao, E.Y.M. Lo, Incompressible SPH method for simulating Newtonian and non-Newtonian flows with a free surface, *Adv. Water Resour.* 26 (2003) 787–800.
- [6] S. Koshizuka, A. Nobe, Y. Oka, Numerical analysis of breaking waves using the moving particle semi-implicit method, *Int. J. Numer. Methods Fluids* 26 (1998) 751–769.
- [7] A. Khayyer, H. Gotoh, Modified moving particle semi-implicit methods for the prediction of 2d wave impact pressure, *Coast. Eng.* 56 (4) (2009) 419–440.
- [8] X.Y. Hu, N.A. Adams, An incompressible multi-phase SPH method, *J. Comput. Phys.* 227 (1) (2007) 264–278.

- [9] M. Asai, A.M. Aly, Y. Sonoda, Y. Sakai, A stabilized incompressible SPH method by relaxing the density invariance condition, *J. Appl. Math.* 2012 (2012) 139583.
- [10] K. Szewc, J. Pozorski, J.-P. Minier, Analysis of the incompressibility constraint in the smoothed particle hydrodynamics method, *Int. J. Numer. Methods Eng.* 92 (4) (2012) 343–369.
- [11] R. Xu, P. Stansby, D. Laurence, Accuracy and stability in incompressible SPH (ISPH) based on the projection method and a new approach, *J. Comput. Phys.* 228 (18) (2009) 6703–6725.
- [12] F. Colin, R. Egli, F.Y. Lin, Computing a null divergence velocity field using smoothed particle hydrodynamics, *J. Comput. Phys.* 217 (2) (2006) 680–692.
- [13] S.J. Lind, R. Xu, P.K. Stansby, B.D. Rogers, Incompressible smoothed particle hydrodynamics for free-surface flows: a generalised diffusion-based algorithm for stability and validations for impulsive flows and propagating waves, *J. Comput. Phys.* 231 (2012) 1499–1523.
- [14] C. Jog, *Foundations and Applications of Mechanics: Continuum Mechanics*, vol. 1, CRC Press, 2002.
- [15] J.J. Monaghan, Smoothed particle hydrodynamics, *Rep. Prog. Phys.* 68 (8) (2005) 1703.
- [16] M. Liu, G. Liu, K. Lam, Constructing smoothing functions in smoothed particle hydrodynamics with applications, *J. Comput. Appl. Math.* 155 (2) (2003) 263–284.
- [17] P. Nair, G. Tomar, An improved free surface modeling for incompressible SPH, *Comput. Fluids* 102 (2014) 304–314.
- [18] H. Wendland, Piecewise polynomial, positive definite and compactly supported radial functions of minimal degree, *Adv. Comput. Math.* 4 (1) (1995) 389–396.
- [19] U. Ghia, K. Ghia, C. Shin, High-Re solutions for incompressible flow using the Navier–Stokes equations and a multigrid method, *J. Comput. Phys.* 48 (3) (1982) 387–411.
- [20] A. Leroy, D. Violeau, M. Ferrand, C. Kassiotis, Unified semi-analytical wall boundary conditions applied to 2-D incompressible SPH, *J. Comput. Phys.* 261 (2014) 106–129.